Ultrafast laser-driven Rabi oscillations of a trapped atomic vapor

Han-gyeol Lee, Hyosub Kim, and Jaewook Ahn*

Department of Physics, KAIST, Daejeon 305-701, South Korea
**Corresponding author: jwahn@kaist.ac.kr*

Received October 30, 2014; revised January 5, 2015; accepted January 5, 2015;
posted January 9, 2015 (Doc. ID 225921); published February 6, 2015

We consider the Rabi oscillation of an atom ensemble of Gaussian spatial distribution interacting with ultrafast laser pulses. Based on an analytical model calculation, we show that its dephasing dynamics is solely governed by the size ratio between the atom ensemble and the laser beam, and that every oscillation peak of the inhomogeneously broadened Rabi flopping falls on the homogeneous Rabi oscillation curve. The results are verified experimentally with a cold rubidium vapor in a magneto-optical trap. As a robust means to achieve higher-fidelity population inversion of the atom ensemble, we demonstrate a spin-echo type $R_x(\pi/2)R_y(\pi)R_x(\pi/2)$ composite interaction as well.

OCIS codes: (320.7085) Ultrafast information processing; (320.5540) Pulse shaping.
http://dx.doi.org/10.1364/OL.40.000510

Rabi oscillation is a fundamental concept in physics with a significant pedigree first discovered in nuclear magnetic resonance (NMR) [1–3] and later extended to atomic physics and quantum optics [4,5]. In the presence of an oscillatory driving field $E(t) = A(t)\cos(\omega t)$, a two-state quantum system undergoes a cyclic change of Bloch vector $\boldsymbol{\rho} = (\sin\theta\cos\phi, \sin\theta\sin\phi, \cos\theta)$ manifested by the precession dynamics $d\boldsymbol{\rho}/dt = \Omega \times \boldsymbol{\rho}$ about an effective torque $\Omega = (-\mu A(t)/2\hbar, 0, \delta)$, where μ is the transition dipole moment between the two energy states, $A(t)$ is the field envelope, and δ is the frequency detuning under the slowly-varying envelope approximation [4]. This generic feature of Rabi oscillation is universally found in a vast variety of material systems ranging from atoms and molecules [6–10] to bulk semiconductors [11], quantum wells and dots [12–15], graphene [16], surface plasmons [17], superconducting quantum devices [18,19], diamond nitrogen-vacancy centers [20], Bose–Einstein condensates [21], and so on.

When we consider an ultrafast-laser induced Rabi oscillation of a two-level atom, the dynamics of the excited state probability, which we may refer to as single-atom Rabi oscillation (SARO), is represented by

$$P(\Theta_o) = \sin^2\frac{\Theta_o}{2}, \tag{1}$$

where Θ_o is the pulse area defined by $\Theta_o = \int \mu A(t)\mathrm{d}t/\hbar$. Since the pulse area is subject to both the pulse duration and the electric-field envelope, Rabi oscillations of an ultrashort time scale can be implemented by ultrafast optical interaction at a sufficiently strong laser intensity regime. However, the spatial extent of the laser beam over the laser–atom interaction region inevitably causes inhomogeneous broadening that often leads to a complete wide out of the oscillatory behavior. To overcome this problem, homogenizing the spatial profile of the laser beams [22,23], limiting the detection region [24], and adapting a chirped laser interaction [25] have been considered.

This Letter aims to present a quantitative analysis of the inhomogeneously broadened Rabi oscillation. For this, we use the atom ensemble localized in a magneto-optical trap (MOT) [26] and make it interact with ultrafast laser pulses. As a theoretical model to investigate the spatially inhomogeneous interaction, we consider a Gaussian laser beam propagating along the z direction. The pulse area in Eq. (1) is then represented in the cylindrical coordinate system as

$$\Theta(r,z) = \Theta_o\frac{w_o}{w(z)}e^{-r^2/w(z)^2} = \Theta_z e^{-r^2/w(z)^2}, \tag{2}$$

where $r = \sqrt{x^2+y^2}$, $w(z)$ is the beam waist at z, $w_o = w(0)$ is the minimal beam waist, Θ_o is the maximal pulse area, and $\Theta_z = w_o\Theta_o/w(z)$. When we assume the atom density profile in the MOT is also a Gaussian, i.e., $\rho(r,z) = \rho_o e^{-(r^2+z^2)/w_a^2}$, the excitation probability averaged over the entire atom ensemble, $\langle P(\Theta_o)\rangle = \int P(r,z;\Theta_o)\rho(r,z)\mathrm{d}V/\int\rho(r,z)\mathrm{d}V$, which we may call the ensemble–atom Rabi oscillation (EARO), is then given by

$$\begin{aligned}\langle P(\Theta_o)\rangle &= \frac{2}{\sqrt{\pi}w_a^3}\int_{-\infty}^{\infty}\mathrm{d}z\int_0^{\infty}\mathrm{d}r r e^{\frac{-(r^2+z^2)}{w_a^2}}\sin^2\frac{\Theta(r,z)}{2}\\ &= \frac{1}{\sqrt{\pi}w_a^3}\int_{-\infty}^{\infty}\mathrm{d}z w^2 e^{-z^2/w_a^2} f(\Theta_z),\end{aligned} \tag{3}$$

where $f(\Theta_z) = \int_0^{\Theta_z}(\Theta/\Theta_z)^{w^2/w_a^2}\sin^2(\Theta/2)\mathrm{d}\Theta/\Theta$. Figure 1(a) shows the numerical calculation of EARO in Eq. (3) for various size ratios w_o/w_a, which is compared with SARO in Eq. (1). The peak shift indicated by two arrows is explained by the distributions of the pulse areas Θ and the Bloch sphere locations, respectively, in Figs. 1(b) and 1(c).

Strikingly every EARO peak appears coincident with the SARO curve. The locations of the EARO peaks can be found from the condition

$$\frac{d\langle P\rangle}{d\Theta_o} = \frac{1}{\sqrt{\pi}w_a^3}\int_{-\infty}^{\infty}\mathrm{d}z w^2 e^{-z^2/w_a^2} f'\frac{d\Theta_z}{d\Theta_o} = 0. \tag{4}$$

It is straightforward to show that $f(\Theta_n) = (w_a/w)^2\sin^2\Theta_n/2$ for those Θ_n terms that satisfy $f' = 0$. Therefore, Eq. (3) at $\Theta = \Theta_n$ results in

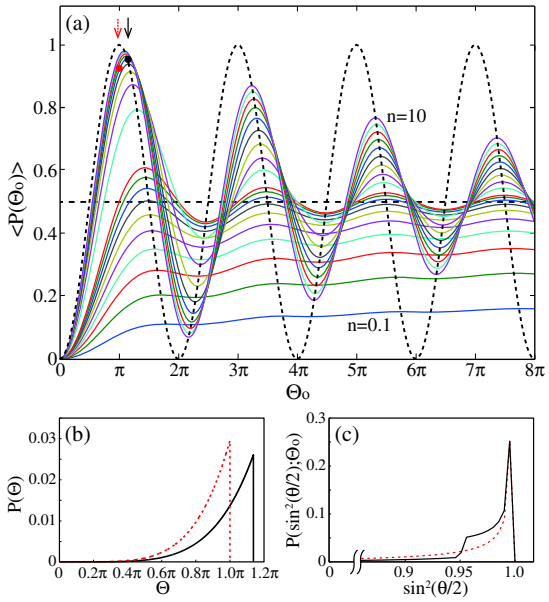

Fig. 1. (a) Ensemble-atom Rabi oscillation in Eq. (3) for various size ratios $w_o/w_a = \sqrt{n}$ for $n = 0.1, 0.2, \ldots, 0.9$ and $1, 2, \ldots, 10$ (from the bottom to the top). Dotted line represents the single-atom Rabi oscillation in Eq. (1); (b)–(c) atom probability distributions, at the marked points from the EARO curve for $w_o/w_a = \sqrt{6}$ in (a), plotted as a function of $\Theta(r, z; \Theta_o)$, the pulse area; (c) atom probability distributions, at the marked points from the EARO curve for $w_o/w_a = \sqrt{6}$ in (a), plotted as a function of θ, the polar angle of the Bloch vector.

$$\langle P(\Theta_n)\rangle = \sin^2\frac{\Theta_n}{2}, \tag{5}$$

which result proves that all EARO peaks are located on the SARO curve.

Experiments were performed with atomic rubidium (^{85}Rb) in a MOT [27,28] as shown in Figs. 2(a) and 2(b). The $5S_{1/2}$ and $5P_{1/2}$ energy states are the ground and excited states, respectively, of the two-level system. The atoms were initially prepared in $F = 3$ hyperfine level of $5S_{1/2}$ by the MOT, and a π-polarized laser pulse induced $\Delta m_F = 0$ transition to $F' = 2$ and 3 of $5P_{1/2}$. The excited and ground states of the combined hyperfine levels formed an effective two-level system, for a ultrafast laser interaction with a moderated laser bandwidth [28,29]. The atomic transition was driven by ultrafast laser pulses from a Ti:sapphire laser amplifier that produced 250 fs short pulses at a repetition rate of 1 kHz. The pulse energy of up to 20 μJ corresponded to the pulse area Θ_o up to 5π. The laser spectrum was centered at $\lambda = 794.7$ nm, the resonant wavelength of the $5S_{1/2} \rightarrow 5P_{1/2}$ transition, and the spectral bandwidth was $\Delta\lambda = 3$ nm (FWHM). The laser pulse was focused on the atom cloud by a $f = 500$ mm lens, and the beam size at the atom cloud was adjusted by translating the lens. The detection of the excited atom population was carried out by photo-ionization as shown in Fig. 2(c). The probing UV pulse for the photo-ionization was prepared by frequency-doubling of a fraction of the main pulse via second-harmonic generation. The beam size of the probing UV pulse was adjusted by another lens $f = 300$ mm. Both laser pulses were combined after the lenses by a dichroic

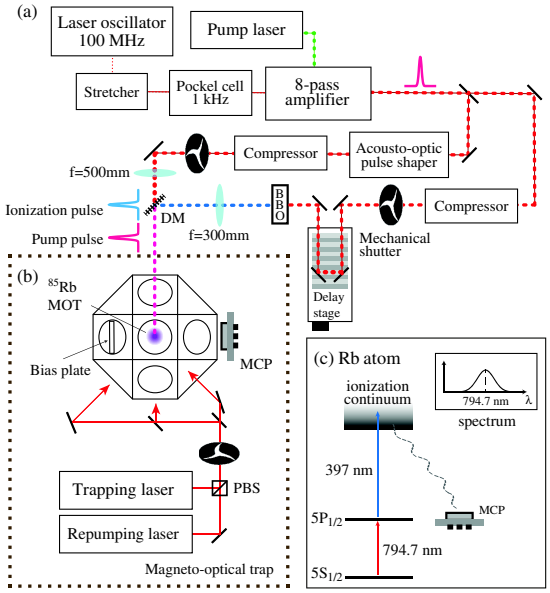

Fig. 2. (a) Schematic diagram of the experimental setup. Ultrafast laser pulses were split into two pulses, one for Rabi oscillation and the other frequency-doubled for atom ionization. Both pulses were independently focused and delivered to the MOT by a dichroic mirror (DM); (b) schematic diagram of the ^{85}Rb MOT chamber. Trapping and re-pumping laser beams were adjusted to vary the atom cloud size from 250 to 500 μm [31]; (c) energy level diagram of the Rb atom and the laser spectrum. Atoms in the excited $5P_{1/2}$ state were photo-ionized and Rb^+ ions were transferred by bias electric plates and measured by a micro-channel plate detector (MCP).

mirror and collinearly delivered to the atom cloud. The time difference controlled by a delay stage between the main and probing pulses was fixed to 10 ps, 1000 times smaller than the decay time of the Rb excited state [30].

The overall experiment of our work was controlled by three mechanical shutters and a delay generator (SRS, DG645), and each experiment was operated at 2 Hz repetition. Atoms were first prepared by turning on the MOT for 500 ms by a mechanical shutter in Fig. 2(b), then the atoms were interacted with the ultrafast laser pulse, before finally being photo-ionized by the probing UV pulse, respectively, controlled by the shutters in Fig. 2(a). The excited-state probability was estimated by comparing the fluorescence image counting of the atoms in the MOT and the ion count. Figure 3 shows the main experimental result, which clearly exhibits the seemingly decay-like oscillatory behavior. The previous analysis on the ensemble–atom laser interaction predicts that such behavior is the spatially averaged Rabi oscillation. The agreement of the numerical calculation by Eq. (3) and the experimental result is excellent. It is noted, however, that the discrepancy between them is evident in particular for a high pulse-area exceeding $\Theta_o = 3\pi$ and also for a higher spatial inhomogeneity in Fig. 3(c) for $w_o/w_a = 1$ than the others. As a cause of the error, we can consider the three-photon ionization directly by the main laser pulse in addition to the one-photo ionization by the probing UV pulse. Such effect is however already systematically taken into account in the data analysis, and the error is estimated less than 2% in the given range of pulse area. The main reason for the discrepancy is the axis

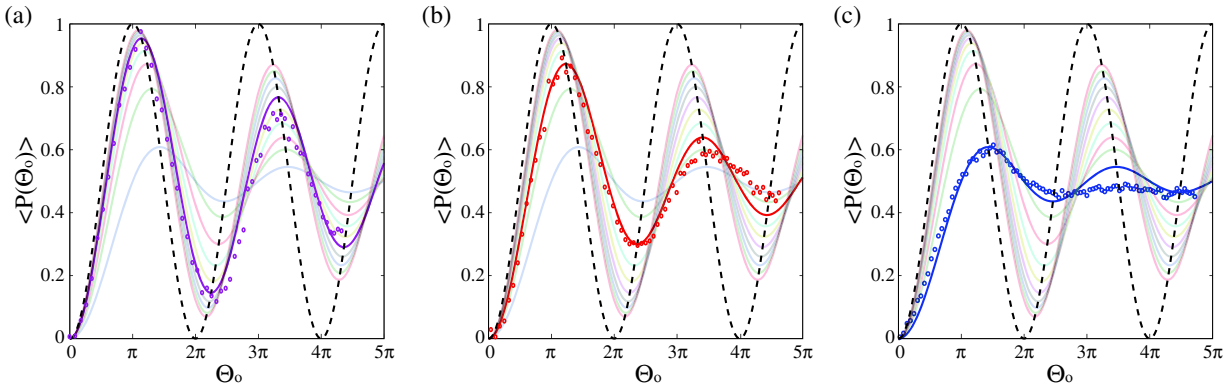

Fig. 3. Experimental result of ensemble-atom Rabi oscillations: (a) laser beam width (w_o) was 2.5 times of the atom cloud size (w_a) or $w_o = 2.5w_a$; (b) $w_o = 1.7w_a$; and (c) $w_o = w_a$. Highlighted line in (a)–(c) illustrates the calculation for the closest integer $(w_o/w_a)^2$ that corresponds to $(w_o/w_a)^2 = 6$, $(w_o/w_a)^2 = 3$, and $(w_o/w_a)^2 = 1$, respectively.

misalignment of at most 50 μm between the laser and the atom cloud, not to mention the imperfect shape of the atom cloud. Our calculation predicts the case in Fig. 3(c) exhibits a total 5% of error. It is noted that the ratios of the adjacent peaks are uniquely determined as a function of the size ratio w_o/w_a, the result of which can be used as an alternative means to calibrate the excited-state probability of the atom ensemble.

In the second experiment of our work, we considered an spin-echo-type interaction to achieve a higher-fidelity Rabi oscillation. We tested the three-pulse composite consisting of two $\pi/2$ rotations about the x axis and a π rotation about the y axis, or $R_x(\pi/2)R_y(\pi)R_x(\pi/2)$, which sequence of pulses is designed in NMR to correct errors caused by pulse-area fluctuation [32,33]. The π-rotation $R_y(\pi)$ about the y axis in the middle corrects the rotation error of the pair of $\pi/2$ rotations $R_x(\pi/2)^2$. In our work, we used the three-pulse composite to reduce the spatial inhomogeneity in the ensemble–atom laser interaction. To make the three pulses of the specific amplitude and phase coding, we used an acousto-optic pulse shaper as shown in Fig. 2(a), and the accurate control of the pulses was checked by *in-situ* autocorrelation measurement [34]. Figure 4 shows the result of the pulse composite experiment. The first-order corrections of the pulse area Θ_o for the π and $\pi/2$ pulses in an ensemble-atom experiment are, respectively, given by $\pi + \alpha$ and $\pi/2 + \beta$, where α and β are determined by the size ratio w_o/w_a. The experiment was thus performed by a pulse sequence $R_x(\pi/2 + \alpha)R_y(\pi + \beta)R_x(\pi/2 + \alpha)$, and the excited-state population is plotted in Fig. 4 as a function of $\Theta_o = \pi + 2\alpha = \pi + \beta$ by fixing $\beta = 2\alpha$ for the experimental convenience. The result in Fig. 4 clearly demonstrates 15% of increase at the first peak of the oscillation by the composite pulse (black circles) compared to the oscillation by the single pulse (red boxes). The robustness of the composite pulse scheme manifested by the broadened oscillation peak around the π rotation is also clearly observed in Fig. 4. It is straightforward to show that the excited state probability for a single-atom excitation is given by $P_e(\Theta_o) = 1 - \cos^4\frac{\Theta_o}{2}$ for the composite pulse, which results in a broader peak shape around $\Theta_o = \pi$ than $\sin^2(\Theta_o/2)$ for a single pulse in Eq. (1).

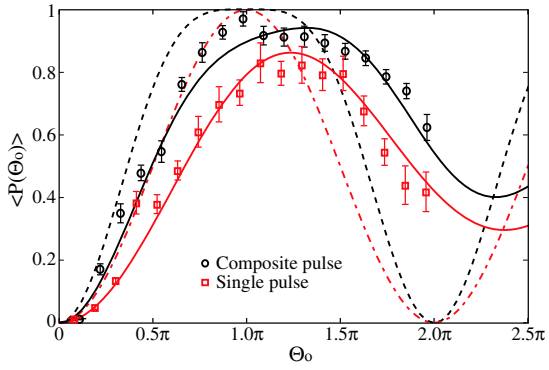

Fig. 4. Composite-pulse experiment of ensemble-atom Rabi oscillation. For an atom ensemble of the size 1.7 times smaller than a laser beam (i.e., $w_o = 1.7w_a$), the excited-state population for the composite-pulse operation $R_x(\Theta_o/2)R_y(\Theta_o)R_x(\Theta_o/2)$ was measured and plotted in black circles. In comparison, the single pulse experiment $R_x(\Theta_o)$ was plotted in red boxes. Solid lines represent the corresponding numerical calculations, when the spatial inhomogeneity of the ensemble-atom experiment is taken into account. Dotted lines are for the spatially homogeneous case (i.e., $w_o \gg w_a$), when the theoretical formulas are given by $1 - \cos^4(\Theta_o/2)$ (black) for the composite pulse and $\sin^2(\Theta_o/2)$ (red) for single pulses, respectively.

In summary, we have investigated Rabi oscillations of a spatially confined atom ensemble in a magneto-optical trap strongly driven by focused femtosecond laser pulses. Analytical theory has predicted that the peaks of the ensemble-atom Rabi oscillations are uniquely determined by the size ratio between the atom ensemble and the laser beam, and the result has been confirmed experimentally. Furthermore, the fidelity enhancement of the atom-ensemble Rabi-flopping has been demonstrated by the proof-of-principle experiment with the spin-echo-type operation $R_x(\pi/2)R_y(\pi)R_x(\pi/2)$.

This work was supported by Samsung Science and Technology Foundation (SSTF-BA1301-12). The cold atom apparatus was constructed in part supported by the Basic Science Research Program (2013R1A2A2A05005187) through the National Research Foundation of Korea.

References

1. I. I. Rabi, J. R. Zacharias, S. Millman, and P. Kusch, Phys. Rev. **53**, 318 (1938).

2. I. I. Rabi, Phys. Rev. **51**, 652 (1937).
3. A. Abragam, *Principles of Nuclear Magnetism* (Oxford University, 2002).
4. L. Allen and J. H. Eberly, *Optical Resonance and Two-Level Atoms* (Dover, 1987).
5. M. O. Scully and M. S. Zubiary, *Quantum Optics* (Cambridge University, 1997).
6. E. T. Jaynes and F. W. Cummings, Proc. IEEE **51**, 89 (1963).
7. G. Rempe, H. Walther, and N. Klein, Phys. Rev. Lett. **58**, 353 (1987).
8. M. Brune, F. Schmidt-Kaler, A. Maali, J. Dreyer, E. Hagley, J. M. Raimond, and S. Haroche, Phys. Rev. Lett. **76**, 1800 (1996).
9. I. Gerhardt, G. Wrigge, G. Zumofen, J. Hwang, A. Renn, and V. Sandoghdar, Phys. Rev. A **79**, 011402 (2009).
10. G. Wrigge, I. Gerhardt, J. Hwang, G. Zumofen, and V. Sandoghdar, Nat. Phys. **4**, 60 (2008).
11. F. Rossi and T. Kuhn, Rev. Mod. Phys. **74**, 895 (2002).
12. T. B. Norris, J.-K. Rhee, C.-Y. Sung, Y. Arakawa, M. Nishioka, and C. Weisbuch, Phys. Rev. B **50**, 14663 (1994).
13. A. Schülzgen, R. Binder, M. E. Donovan, M. Lindberg, K. Wundke, H. M. Gibbs, G. Khitrova, and N. Peyghambarian, Phys. Rev. Lett. **82**, 2346 (1999).
14. T. H. Stievater, X. Li, D. G. Steel, D. Gammon, D. S. Katzer, D. Park, C. Piermarocchi, and L. J. Sham, Phys. Rev. Lett. **87**, 133603 (2001).
15. C.-M. Simon, T. Belhadj, B. Chatel, T. Amand, P. Renucci, A. Lemaitre, O. Krebs, P. A. Dalgarno, R. J. Warburton, X. Marie, and B. Urbaszek, Phys. Rev. Lett. **106**, 166801 (2011).
16. P. N. Romanets and F. T. Vasko, Phys. Rev. B **81**, 241411(R) (2010).
17. E. S. Andrianov, A. A. Pukhov, A. V. Dorofeenko, A. P. Vinogradov, and A. A. Lisyansky, Phys. Rev. B **85**, 035405 (2012).
18. K. R. Patton and U. R. Fischer, Phys. Rev. A **87**, 052303 (2013).
19. J. M. Martinis, S. Nam, J. Aumentado, and C. Urbina, Phys. Rev. Lett. **89**, 117901 (2002).
20. D. A. Golter and H. Wang, Phys. Rev. Lett. **112**, 116403 (2014).
21. M. R. Matthews, B. P. Anderson, P. C. Haljan, D. S. Hall, M. J. Holland, J. E. Williams, C. E. Wieman, and E. A. Cornell, Phys. Rev. Lett. **83**, 3358 (1999).
22. J. Lim, K. Lee, and J. Ahn, Opt. Lett. **37**, 3378 (2012).
23. M. Reetz-Lamour, T. Amthor, J. Deiglmayr, and M. Weidemüller, Phys. Rev. Lett. **100**, 253001 (2008).
24. H. Braun, T. Bayer, C. Sarpe, R. Siemering, R. de Vivie-Riedle, T. Baumert, and M. Wollenhaupt, J. Phys. B **47**, 124015 (2014).
25. S. Zhdanovich, E. A. Shapiro, M. Shapiro, J. W. Hepburn, and V. Milner, Phys. Rev. Lett. **100**, 103004 (2008).
26. W. D. Phillips, Rev. Mod. Phys. **70**, 721 (1998).
27. S. Lee, H. G. Lee, J. Cho, J. Lim, C. Y. Park, and J. Ahn, Phys. Rev. A **86**, 045402 (2012).
28. J. Lim, H. Lee, S. Lee, C. Y. Park, and J. Ahn, Sci. Rep. **4**, 5867 (2014).
29. H. Kim, H. Lee, and J. Ahn, "Ultrafast manipulation of atomic ground hyperfine sublevels," presented at the Optical Society of Korea Summer Meeting, Jeju, Korea, August 25–27, 2014.
30. D. A. Steck, "Rubidium 85 D line data," http://steck.us/alkalidata.
31. G. L. Gattobigio, T. Pohl, G. Labeyrie, and R. Kaiser, Phys. Scripta **81**, 025301 (2010).
32. M. H. Leviti and R. Freeman, J. Magn. Reson. **33**, 473 (1979).
33. W. Rakreungdet, J. H. Lee, K. F. Lee, B. E. Mischuck, E. Montano, and P. S. Jessen, Phys. Rev. A **79**, 022316 (2009).
34. R. Trebino, K. W. DeLong, D. N. Fittinghoff, J. N. Sweetser, M. A. Krumbügel, and B. A. Richman, Rev. Sci. Instrum. **68**, 3277 (1997).